Int. J. Multiphase Flow Vol. 14, No. 1, pp. 47–65, 1988
Printed in Great Britain.

0301-9322/88 $3.00 + 0.00

A HYDRODYNAMIC MODEL FOR TWO-PHASE FLOW THROUGH POROUS MEDIA

V. X. TUNG and V. K. DHIR

Mechanical, Aerospace and Nuclear Engineering Department, School of Engineering and Applied Science, University of California, Los Angeles, Los Angeles, CA 90024, U.S.A.

(*Received* 1 *October* 1986; *in revised form* 25 *August* 1987)

Abstract—A hydrodynamic model has been developed to predict void fraction and pressure gradient for one-dimensional two-phase flow through porous media. The model includes discussion of flow regimes and their relationship with flow and porous layer configurations. The particle–gas drag, particle–liquid drag and liquid–gas interfacial drag are then evaluated theoretically from the flow configuration associated with each flow regime. The above drag models are then employed in conjunction with force balances on the two phases to obtain the void fraction and pressure gradient as functions of liquid and gas superficial velocities. Results are found to agree very favorably with existing experimental data obtained in both co-current and counter-current flow conditions.

It has also been found that this hydrodynamic model is capable of fully describing essential features of the flooding phenomenon observed in counter-current flow of immiscible fluids. Furthermore, counter-current flooding limits predicted using this hydrodynamic model are found to agree well with existing correlations in the literature. Seemingly conflicting experimental observations reported by various authors on the behavior of void fractions and pressure drops near the flooding limit can also be resolved by the present model.

1. INTRODUCTION

Basic understanding of two-phase flow through porous media is of interest in many nuclear, chemical and geophysical applications. For example in light water reactors one of the accident scenarios considered in safety evaluation is the degraded core accident. In-place recovery from a degraded core accident depends on the rate at which energy can be removed. Under a constant pressure difference one of the major parameters controlling the coolant flowrate and hence energy removal rate is the two-phase pressure drop. Therefore, a reliable hydrodynamic model for two-phase flow through porous media is of utmost important in the assessment of debris coolability. In the event of prolonged overheating of the debris, quenching must first be accomplished before the quasi-steady heat removal rate from the debris can be established. Generally, quenching may be attempted either by dumping coolant on top of the hot debris or by forcing coolant into the debris from below. In either mode of quenching, extensive information on two-phase flow resistance and forced flow boiling heat transfer is required for accurate assessement of debris quenchability.

Several experimental and analytical studies on hydrodynamic aspects of two-phase flow through porous media have been reported in the recent literature. Vasiliev & Maiarov (1979) analyzed heat transfer and pressure drop in forced flow cooling of volumetrically heated porous medial. In their model, two-phase pressure drop was obtained by treating the two-phase mixture as a single fluid with properties obtained by an averaging process which included the flow quality. Such a model is speculative at best and offers no insight into other aspects of the two-phase flow process. Naik & Dhir (1982) employed a separated flow model to evaluate two-phase pressure drop. In their model, the void fraction was correlated as a function of the flow quality and mass flowrate. The model worked reasonably well for a water–steam mixture at atmospheric pressure. However, it under-predicted pressure drop for fluid mixtures with a higher vapor liquid density ratio, as has been shown by Tung *et al.* (1983). Tutu *et al.* (1983) pointed out the importance of the interfacial drag for porous layers composed of coarse particles. However, their model of the interfacial drag showed a large discrepancy with respect to their own experimental results. Schulenberg & Muller (1984) correlated particle drag using the concept of relative permeabilities. The interfacial drag was correlated with a parameter containing capillary force. However, at void fractions >0.4 their data showed a large scatter with respect to the correlation. Chu *et al.* (1983) obtained extensive

data on pressure drop and void fraction in co-flow and counter-flow of air and water. In their work a semi-empirical drift flux model was developed to predict void fractions as a function of liquid and gas flowrates. Expressions for relative permeabilities were also given by Chu *et al.* However, different relative permeabilities had to be employed for co-current and for counter-current flows to fit the pressure drop data. The drift flux model of Chu *et al.* was later improved by Dhir (1984) to include a correction factor due to the motion of bubbles around surfaces of particles. Even though this approach worked well for co-current flows it generally resulted in over-prediction of the flooding limits when applied to counter-current flows.

Early studies on counter-current flooding were motivated by potential applications in absorption towers employed in the chemical industry. Sherwood *et al.* (1938) performed an experimental study on flooding velocities in packed columns. They found that for large-size packing materials, the flooding velocities of the two phases could be correlated with dimensionless groups based on inertia of the fluid streams. Subsequent studies by Lobo *et al.* (1946) and Dell & Pratt (1951) resulted in similar findings. Wallis (1969) compiled all the data and arrived at a much simpler correlation which enjoyed wide acceptance in the chemical industry. Wallis's correlation however tended to under-predict the flooding limits observed in columns packed with spherical particles.

Marshall & Dhir (1984) performed an experimental study of counter-current flow in porous media composed of spherical particles. Based on their flooding data they arrived at a correlation for the flooding limits. The functional form of their correlation is similar to that of Wallis except that the empirical constant is about 15% higher. Schrock *et al.* (1984) also performed similar experiments in a different range of liquid velocities and obtained another correlation which is slightly different from the correlations of Wallis (1969) and Marshall & Dhir (1984). It should be pointed out that in all of the flooding correlations nondimensionalization of the velocities is based on the inertia of the two phases and the specific surface area of the material forming the porous layer.

Since the counter-current flooding limit generally controls dryout heat fluxes in porous media, considerable interest has been generated recently over the possibility of employing hydrodynamic models in predicting dryout. Hardee & Nilson (1977) proposed a laminar flow model for two-phase flow in porous medial composed of small particles, while Lipinski (1981) proposed a turbulent flow model for larger particles. In their models no serious attempt was made to model the interfacial drag between the two phases. Jones *et al.* (1980) employed an optimizing process with assumed relative permeabilities to obtain void fractions at flooding in their laminar annular flow model. Dhir & Barleon (1981) on the other hand employed a geometric argument to obtain void fractions at flooding. Applicability of the above models is restricted to calculation of dryout heat fluxes. Lipinski (1984) and Schrock *et al.* (1984) have predicted dryout heat fluxes using their limiting flow correlations which include the concept of relative permeabilities of the two phases.

Although predictions made from most of the above models compare reasonably well with dryout heat flux data, the models cannot be used for flow conditions different than that at the flooding limit. The models also fail when extended to co-flow conditions. The main reason for deficiency in these models is the lack of mechanistic details of the drags experienced by the different phases, including the interfacial drag.

The objective of the present work is to develop a one-dimensional model for two-phase flow in porous media made up of large size particles. The model includes submodels for flow regime transitions and the particle–liquid, particle–gas and liquid–gas interfacial drags. A verification of the model is sought through comparison with available co-current flow data. The model is also used to predict the flooding limit observed in counter-current flow through porous media.

2. ANALYSIS

Prior to the modeling of two-phase flow, it is necessary that the flow patterns and their geometrical configurations be identified. Chu *et al.* (1983), based on their visual observations in porous media composed of large-size particles ($D_p \geqslant 6$ mm), reported a distinct change in flow patterns with an increase in the void fraction. At low void fraction, bubbly flow existed in the pores. As the void fraction was increased with increasing gas superficial velocity, bubbly flow gave way to slug flow and eventually the flow became annular. Figure 1 shows sketches of the observed flow

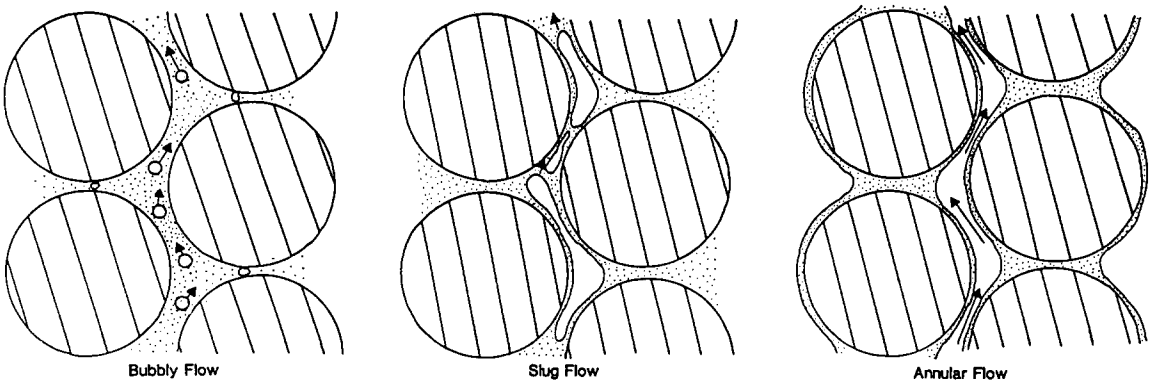

Figure 1. Sketches of flow patterns in different flow regimes.

patterns. The flow patterns appear to have features very similar to those observed in tubes. It should be noted that the flow patterns shown in figure 1 are obtained with an adiabatic flow of gas and liquid. In a boiling system the flow configuration can differ substantially if film boiling is present on the particles, and to a limited extent in the presence of nucleate boiling.

Flow Regimes

A flow regime map based on the early UCLA data was presented by Dhir (1984). Such a flow regime map could be used to guide the evaluation of various drag forces. However, in this work different flow regimes, namely bubbly flow, slug flow and annular flow, along with the associated transitions are first modeled.

Bubbly flow

At low void fractions the flow configuration is characterized by the motion of discrete bubbles. Initially, the bubbles tend to adhere to the particles' surface and therefore travel upward along the surface of the particles. Although continuous breakup and reformation of bubbles take place, the bubbles can be assumed to be spherical in shape with an average diameter D_b. The void fraction, α_0, corresponding to the maximum number of bubbles supported by the surface of particles can be obtained through a simple geometrical model. The model, given in detail in the appendix, yields the following expression for this void fraction:

$$\alpha_0 = \frac{\pi}{3}\frac{(1-\epsilon)}{\epsilon}\gamma(1+\gamma)[6\eta - 5(1+\gamma)] \quad \text{as long as} \quad \alpha_0 \geq 0. \tag{1}$$

In the above equation γ and η are given as

$$\gamma = \frac{D_b}{D_p} \tag{2}$$

and

$$\eta = \left[\frac{\pi\sqrt{2}}{6(1-\epsilon)}\right]^{1/3}. \tag{3}$$

The bubble diameter D_b employed in [2] is controlled by surface tension and buoyancy. A detailed discussion on the calculation of D_b can be found at the end of this section.

After maximum packing at the particle surface has occurred, the bubbles will start to move straight through the pores. At a still higher void fraction α_l the bubbles will merge to form slugs. The void fractions α_l can be deduced (see the appendix) from the work of Marshall & Dhir (1984) on porosity of a binary mixture of different size particles. The expression for void fraction at the onset of bubble merger is obtained as

$$\alpha_l = 0.6(1-\gamma)^2 \quad \text{as long as} \quad \alpha_l < 0.3. \tag{4}$$

Since in the limit as $\gamma \to 0$ the flow in the pores will be similar to that in a tube, the transition

void fraction can not exceed that in the tube. Hence applicability of [4] is limited to a void fraction <0.3.

Bubbly-slug flow

At void fraction α_1 some bubbles will start to merge into slugs. The transition from bubbly to slug flow, however, is a smooth one and there is a range of void fraction in which bubbles and slugs co-exist. The upper bound of this region can be obtained by assuming that transition is complete when the void fraction corresponds to the lightest packing of slugs, i.e. a cubic array. In this conceptualization the slugs are replaced by equivalent volume spheres which fill the pore space and arrange themselves in a cubic array. The void fraction, α_2, corresponding to this arrangement is obtained from Scheidegger (1960) as

$$\alpha_2 = \frac{\pi}{6}. \qquad [5]$$

Therefore the bubbly to slug flow transition will end at a void fraction of $\pi/6$.

Pure slug flow

The regime of pure slug flow begins at void fraction α_2. As the void fraction increases the slugs are packed more densely together. However, there is an upper value α_3 beyond which the slugs themselves will merge to form continous gas paths. At this void fraction transition to annular flow begins. In obtaining the void fraction corresponding to this transition it is conceptualized that the slugs are replaced by spheres which fill the pores.

Even though the packing of slugs may be different from the packing of spheres, it is the center-to-center distance between two adjacent slugs which determines the void fraction at merger. This distance is at a minimum when two slugs are parallel to one another. A maximum is reached when they are perpendicular to each other. On average, this distance may be represented by the diameter of a sphere whose volume is the same as that of a slug. These equivalent spheres acquire a natural packing while filling the pore space. The void fraction representative of this natural packing is simply obtained as

$$\alpha_3 = 0.6. \qquad [6]$$

Slug-annular flow

Departure from pure slug flow begins at void fraction α_3. The transition to annular flow is also a smooth one with an upper bound α_4. The void fraction α_4 is taken to be that corresponding to the densest possible packing of the pore space by the equivalent spheres. The densest packing occurs when the equivalent spheres are arranged in a rhombo-hedral array, i.e. slugs have to merge completely if more gas is present in the pores. Thus onset of annular flow will occur at

$$\alpha_4 = \frac{\pi\sqrt{2}}{6}. \qquad [7]$$

Pure annular flow

At void fractions higher than α_4, the slugs merge completely to form continuous gas flow paths. The liquid then flows along the surface of the particles as a thin film. At very high gas flowrates it is conceivable that some liquid may detach from the liquid–gas interface and appear as entrained droplets. However, this will occur at void fractions very close to unity. Therefore, in the present model, pure annular flow is assumed to persist up to $\alpha \cong 1$.

Bubble and slug size

For the large particles considered in this paper, the pore size is much larger than the bubble diameter. Therefore, the bubble diameter is generally determine by surface tension and buoyancy. In the present work, the value of D_b is taken as

$$D_b = 1.35\left[\frac{\sigma}{g(\rho_L - \rho_G)}\right]^{1/2}, \qquad [8]$$

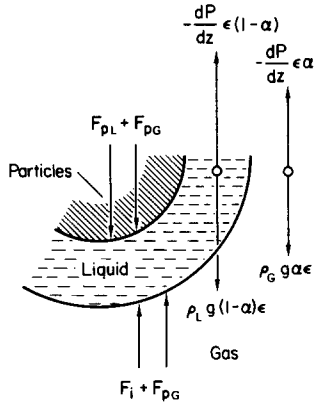

Figure 2. Forces acting on the two phases.

where the constant of proportionality 1.35 is determined from photographs taken during experiments performed by Chu *et al.* (1983). Similarly, it was observed from these photographs that the lateral dimension of the slug is also given by [8]. The slug length, on the other hand, is dependent on a delicate balance between inertia force, which tends to break it up, and surface tension force, which tends to hold it together. However, a detailed analysis of the slug length is beyond the scope of the present work. Therefore, the length of the slug will be taken from above-mentioned photographs as

$$\frac{L_b}{D_b} = 8. \qquad [9]$$

Forces on the Two Phases

Gas and liquid flow configurations in a unit volume cell representing cross-sectionally averaged flow conditions are shown in figure 2. Even though the annular flow configuration is shown, the force balances obtained should be equally applicable to other flow regimes.

Since particles are not in direct contact with the gas, their effect on the gas phase is strictly restricted to what is felt across the liquid layer. Therefore, the actual interfacial drag between the two flowing phases is broken into two components as shown in figure 2. The first component, F_{pG}, is opposed by an equal and opposite force applied by the particles on the other side of the liquid layer. In this context, F_{pG} can be viewed as a particle–gas drag. The second component, F_i, is the drag force on the gas as a result of relative motion between the two phases. If α is the active void fraction,† the force balance on the gas phase is given by

$$-\frac{dP}{dz}\alpha\epsilon = \rho_G g\alpha\epsilon + F_{pG} + F_i. \qquad [10]$$

Similarly, the particle drag on the liquid can be broken into two components F_{pG} and F_{pL}. The first component F_{pG} is simply a reaction to the force by which the gas pushes the liquid against the particles. The second component F_{pL} represents the force acting on the particles due to the liquid motion. The force balance on the liquid then yields

$$-\frac{dP}{dz}(1-\alpha)\epsilon = \rho_L g(1-\alpha)\epsilon + F_{pL} - F_i. \qquad [11]$$

It should be noted that F_{pG}, F_{pL} and F_i represent the drag forces per unit of total bed volume. Since the size of the particles considered in this work is large, the capillary effect will be confined to a very small fraction of the pore volume and hence is neglected. Because of interfacial tension, the pressure in the gas phase will be slightly higher than that in the liquid. However, the pressure

†It has been observed by Chu *et al.* (1983) that in porous layers composes of small particles a certain volume of gas remains trapped in the interstitials. However, for the large-size particles considered here the volume of trapped gas will be very small.

difference between gas and liquid will remain constant in the direction of flow. As such, the pressure gradient in the direction of flow is the same for both phases. In [10] and [11], z is the distance in the direction of flow, ϵ is the porosity, ρ_L and ρ_G are the liquid and gas densities, respectively, and g is the gravitational acceleration. By defining the dimensionless variables

$$P^* = \frac{-\frac{dP}{dz}}{g(\rho_L - \rho_G)}, \quad [12]$$

$$F^* = \frac{F}{g\epsilon(\rho_L - \rho_G)} \quad [13]$$

and

$$\rho^* = \frac{\rho_G}{\rho_L}, \quad [14]$$

[10] and [11] become

$$P^*\alpha = \frac{\rho^*\alpha}{(1-\rho^*)} + F^*_{pG} + F^*_i \quad [15]$$

and

$$P^*(1-\alpha) = \frac{(1-\alpha)}{(1-\rho^*)} + F^*_{pL} - F^*_i. \quad [16]$$

Equations [15] and [16] involve five variables and as such three more relationships are needed before these equations can be solved explicitly. In the following sections, models for the three variables F^*_{pG}, F^*_{pL} and F^*_i are presented.

Particle–Gas Drag Model

In single-phase flow, the particle–gas drag force per unit of total bed volume can be obtained from the Kozeny–Carman equation as

$$F_{pG} = -\frac{dP}{dz}\epsilon = \epsilon(a\mu_G j_G + b\rho_G j_G^2), \quad [17]$$

where j_G is the superficial velcoity of the gas based on the total bed area and the constants a and b are defined as

$$a = 150\frac{(1-\epsilon)^2}{\epsilon^3 D_p^2} \quad \text{and} \quad b = 1.75\frac{(1-\epsilon)}{\epsilon^3 D_p}. \quad [18]$$

Since the liquid is always in contact with the particles and F_{pG} is being modeled as the force by which the gas pushes the liquid against the particles, the system of particles and liquid may be considered as an isotropic porous layer with porosity $\epsilon\alpha$. Also, the particle diameter must be corrected for the increase in particle volume due to the liquid layer, yielding an effective diameter of $[(1-\epsilon\alpha)/(1-\epsilon)]^{1/3}D_p$. Using the effective porosity $\epsilon\alpha$ and the corrected particle diameter, parameters a and b become

$$\bar{a} = \frac{a}{\alpha^3}\left(\frac{1-\epsilon\alpha}{1-\epsilon}\right)^{4/3} \quad \text{and} \quad \bar{b} = \frac{b}{\alpha^3}\left(\frac{1-\epsilon\alpha}{1-\epsilon}\right)^{2/3}. \quad [19]$$

In the separated flow (annular flow) model shown in figure 2, gas occupies only $\epsilon\alpha$ volume fraction of the bed. Therefore the r.h.s. of [17] should be multiplied by α. By using $\bar{a}$ and $\bar{b}$ instead of a and b in [17] and multiplying it by α, the particle drag force on the gas in the annular flow regime can be written as

$$F_{pG} = \epsilon\left[\frac{(1-\epsilon\alpha)^{4/3}}{(1-\epsilon)^{4/3}}\frac{a\mu_G j_G}{\alpha^2} + \frac{(1-\epsilon\alpha)^{2/3}}{(1-\epsilon)^{2/3}}\frac{b\rho_G j_G^2}{\alpha^2}\right]. \quad [20]$$

In bubbly and slug flows, the gas follows a tortuous path and has all of the flow area accessible to it. For these flow regimes [17] should not be multiplied by α. Thus for bubbly and slug flows, the particle drag on the gas is given by

$$F_{pG} = \epsilon \left[\frac{(1-\epsilon\alpha)^{4/3}}{(1-\epsilon)^{4/3}} \frac{a\mu_G j_G}{\alpha^3} + \frac{(1-\epsilon\alpha)^{2/3}}{(1-\epsilon)^{2/3}} \frac{b\rho_G j_G^2}{\alpha^3} \right]. \quad [21]$$

Nondimensionalization of [20] and [21] in a manner similar to [13] yields

$$F^*_{pG} = \frac{a^*\mu_G j_G}{k_G} + \frac{b^*\rho_G j_G^2}{\eta_G}, \quad [22]$$

where

$$a^* = \frac{a}{g(\rho_L - \rho_G)}, \quad b^* = \frac{b}{g(\rho_L - \rho_G)} \quad [23]$$

and k_G and η_G are relative permeabilities. The relative permeabilities are defined as:

(i) $0 \leqslant \alpha \leqslant \alpha_3$ (bubbly and slug flows),

$$k_G = \left(\frac{1-\epsilon}{1-\epsilon\alpha} \right)^{4/3} \alpha^3 \quad \text{and} \quad \eta_G = \left(\frac{1-\epsilon}{1-\epsilon\alpha} \right)^{2/3} \alpha^3; \quad [24]$$

(ii) $\alpha_4 \leqslant \alpha \leqslant 1$ (pure annular flow),

$$k_G = \left(\frac{1-\epsilon}{1-\epsilon\alpha} \right)^{4/3} \alpha^2 \quad \text{and} \quad \eta_G = \left(\frac{1-\epsilon}{1-\epsilon\alpha} \right)^{2/3} \alpha^2; \quad [25]$$

(iii) $\alpha_3 < \alpha < \alpha_4$ (transition).

The transition from slug to annular flow occurs as the void fraction increases from α_3 to α_4. In this range of the void fraction, a simplistic approach will be to form a weighting function between [20] and [21]. A smooth transition between the two flow regimes can be obtained by defining the weighting function as

$$W = \xi^2(3 - 2\xi), \quad \text{where} \quad \xi = \frac{\alpha - \alpha_3}{\alpha_4 - \alpha_3}. \quad [26]$$

The relative permeabilities in this transition flow regime then can be given by

$$k_G = \frac{\left(\frac{1-\epsilon}{1-\epsilon\alpha} \right)^{4/3} \alpha^2}{\left(W + \frac{1-W}{\alpha} \right)} \quad \text{and} \quad \eta_G = \frac{\left(\frac{1-\epsilon}{1-\epsilon\alpha} \right)^{2/3} \alpha^2}{\left(W + \frac{1-W}{\alpha} \right)}. \quad [27]$$

The above weighting function W has been chosen such that the relative permeabilities are continuous to the first derivative at the end points.

Particle–Liquid Drag Model

The particle–liquid drag can be modeled in the same manner as the particle–gas drag. However, since the liquid is always in contact with the particles, the particle diameter and the solid fraction term $(1-\epsilon)$ in parameters a and b need not be corrected. Nevertheless, porosity should be multiplied by $(1-\alpha)$. Also, the liquid follows a tortuous path even up to $\alpha \sim 1$ and all of the pore space is accessible to it. As such, the liquid friction pressure drop equation will be similar to [17] for the gas. The dimensionless particle–liquid drag is thus given by

$$F^*_{pL} = \frac{a^*\mu_L j_L}{k_L} + \frac{b^*\rho_L j_L |j_L|}{\eta_L}, \quad [28]$$

where

$$k_L = \eta_L = (1-\alpha)^3. \quad [29]$$

It should be noted that the relative permeabilities defined in this section are employed only to obtain the particle drag on each phase. These should not be confused with the definitions given in Scheidegger (1960), where for co-flow the contributions of particle drag and interfacial drag are lumped together.

Liquid–Gas Interfacial Drag Model

The interfacial drag, F_i, is defined as the total drag on the gas phase per unit volume of the porous layer induced by the relative motion between the two phases. The approach here will be to develop an expression for the drag on a single bubble/slug and then multiply it by the number of bubbles/slugs per unit volume of the porous layer.

Bubbly flow ($0 \leqslant \alpha \leqslant \alpha_1$)

The drag on a single bubble will depend on the velocity of the bubble relative to the two-phase mixture velocity. At very low relative velocities (Stokes flow) viscous effects will dominate. At high relative velocities the main contribution will come from form or inertial drag. In this work an expression applicable over a wide range of relative velocities is obtained by superimposing the two drags. Such an approach gives correct limiting values at the expense of slight inaccuracy at intermediate velocities. The expression for drag on a single bubble is written as

$$F_d = C_v 3\pi D_b \mu_L \left(\frac{j_s}{\epsilon}\right) + \frac{1}{2} C_i \frac{\pi}{4} D_b^2 \rho_m \left(\frac{j_s}{\epsilon}\right)^2. \quad [30]$$

In the above equation C_v and C_i are the viscous and inertial drag coefficients for a single bubble, respectively; ρ_m is the mixture density, defined as

$$\rho_m = \rho_L(1 - \alpha + \rho^*\alpha); \quad [31]$$

and j_s is the drift velocity of the bubble relative to the mixture, given by

$$j_s = j_G \frac{(1-\alpha)}{\alpha} - j_L. \quad [32]$$

For a single bubble in an infinite pool of liquid, the drag coefficient, C_v, has a value of unity, whereas C_i is 0.45 in Newton's regime where inertial drag dominates and the drag coefficient remains constant. The presence of other bubbles, especially when a bubble moves in the wake of another bubble, can influence the drag. The influence, however, will be limited to Newton's regime. Ishii & Chawla (1979) have shown that for flow in tubes, the correction factor to C_i should be $(1-\alpha)^3$. Here it is proposed that this correction factor will also be valid for flow in porous layers composed of large particles. Furthermore, Dhir (1984) has shown that the superficial relative velocity j_s must be multiplied by a geometric factor given by

$$f = \frac{1}{2}(1+\gamma)\ln\left(1 + \frac{2}{\gamma}\right) \quad [33]$$

when bubbles move along the surface of the particles. The number of bubbles per unit volume of the porous layer is given by

$$N = \frac{\alpha\epsilon}{\frac{\pi}{6} D_b^3} \quad [34]$$

By multiplying [30] with [34] and using the correction factors to C_i and j_s, the dimensionless form of the interfacial drag in bubbly flow is obtained as

$$F_i^* = C_v' \frac{\nu_L j_s}{g D_b^2 (1-\rho^*)\epsilon} + C_i' \frac{(1-\alpha+\rho^*\alpha) j_s^2}{g D_b (1-\rho^*)\epsilon^2}, \quad [35]$$

where the coefficients C_v' and C_i' are given as:

$$0 \leqslant \alpha \leqslant \alpha_0,$$

$$C_v' = 18\alpha f \quad [36]$$

and

$$C_i' = 0.34(1-\alpha)^3 \alpha f^2; \quad \alpha_0 \leqslant \alpha \leqslant \alpha_1, \tag{37}$$

$$C_v' = 18(\alpha_0 f + \alpha - \alpha_0) \tag{38}$$

and

$$C_i' = 0.34(1-\alpha)^3(\alpha_0 f^2 + \alpha - \alpha_0). \tag{39}$$

Slug flow ($\alpha_2 \leqslant \alpha \leqslant \alpha_3$)

Slugs generally can be considered as long, thin ellipsoids whose lateral dimension is D_b and whose length is given by [9]. An expression for the drag force on such a slug, which includes both the viscous and inertial components, can be written as

$$F_d = 6.94\pi D_b \mu_L \frac{j_s}{\epsilon} + \frac{1}{2} C_i \frac{\pi}{4} D_b^2 \rho_m \left(\frac{j_s}{\epsilon}\right)^2. \tag{40}$$

The viscous term in [40] is obtained from the solution of Stokes flow around an ellipsoid given by Lamb (1932). Based on available data in the literature, the inertial drag coefficient C_i has been evaluated by Ishii & Chawla (1979) for tube flow as

$$C_i = 9.8(1-\alpha)^3. \tag{41}$$

The number of slugs per unit volume of the porous layer is given by

$$N = \frac{\epsilon\alpha}{\frac{\pi}{6} D_b^2 L_b} = \frac{\epsilon\alpha}{\frac{4}{3}\pi D_b^3}. \tag{42}$$

Since slugs are fairly long and extend beyond a pore length, they do not flow along the particles as do the spherical bubbles at void fractions less than α_0. Consequently, a geometrical correction on j_s is not needed. Multiplication of [40] with [42] yields the following expression for F_i:

$$F_i = 5.21 \frac{\mu_L j_s \alpha}{D_b^2} + \frac{3}{32} C_i \frac{\rho_L (1 - \alpha + \rho^* \alpha)}{D_b} \epsilon\alpha \left(\frac{j_s}{\epsilon}\right)^2. \tag{43}$$

Equation [43] when nondimensionalized using [13] results in an expression for F_i^* identical to [35], where the coefficients C_v' and C_i' are given by

$$C_v' = 5.21\alpha \tag{44}$$

and

$$C_i' = 0.92(1-\alpha)^3\alpha. \tag{45}$$

Bubbly-slug flow ($\alpha_1 \leqslant \alpha \leqslant \alpha_2$)

A smooth transition between bubbly and slug flow can be obtained by defining a weighting function for C_v' and C_i' similar to [26]:

$$W = \xi^2(3 - 2\xi), \quad \text{where} \quad \xi = \frac{\alpha - \alpha_1}{\alpha_2 - \alpha_1}. \tag{46}$$

The interfacial drag in this flow regime can be given by [35] with C_v' and C_i' defined by

$$C_v' = 18(\alpha_0 f + \alpha - \alpha_0)(1 - W) + 5.21\alpha W \tag{47}$$

and

$$C_i' = (1-\alpha)^3\{0.34(\alpha_o f + \alpha - \alpha_0)(1 - W) + 0.92\alpha W\}. \tag{48}$$

Annular flow ($\alpha \geqslant \alpha_4$)

In the annular flow regime, the interfacial drag induced by the relative motion between the two phases can be modeled in a manner similar to the particle–gas drag. However, the reference velocity

must be taken as

$$j_r = j_G - \frac{\alpha}{1-\alpha} j_L \qquad [49]$$

to account for the slip between the two phases. Furthermore, instead of obtaining F_i as the force exerted by the liquid on the gas, one can obtain F_i as the force exerted by the gas on the liquid. Therefore, by employing the modified particle diameter and porosity in the Kozeny–Carman equation and multiplying the resulting pressure gradient by $\epsilon(1-\alpha)$ to account for the flow area of liquid, the interfacial drag F_i can be obtained as

$$F_i = \epsilon(1-\alpha)(\bar{a}\mu_G j_r - \bar{b}\rho_G j_r^2), \qquad [50]$$

where the parameters $\bar{a}$ and $\bar{b}$ are given by [19]. Nondimensionalization of [50] in a manner similar to [13] results in

$$F_i^* = \frac{(1-\alpha)}{\alpha}\left(\frac{a^*\mu_G j_r}{k_G} + \frac{b^*\rho_B j_r^2}{\eta_G}\right) \qquad [51]$$

or

$$F_i^* = \frac{a^*\mu_G}{k_G} j_s + \frac{\alpha}{1-\alpha}\frac{b^*\rho_G}{\eta_G} j_s^2, \qquad [52]$$

where k_G and η_G are given by [25] and j_s is given by [32].

Slug-annular flow ($\alpha_3 < \alpha < \alpha_4$)

In the transition flow regime, the weighting function defined by [26] may also be used to obtain the dimensionless interfacial drag:

$$F_i^* = \left[5.21\alpha\frac{v_L(1-W)}{gD_b^2(1-\rho^*)\epsilon} + \frac{a^*\mu_G}{k_G}W\right] j_s + \left[0.92\alpha(1-\alpha)^3\frac{(1-\alpha+\rho^*\alpha)(1-W)}{\epsilon^2 g D_b(1-\rho^*)} + \frac{\alpha}{1-\alpha}\frac{b^*\rho_G}{\eta_G}W\right] j_s^2, \qquad [53]$$

where k_G and η_G are given by [25].

3. RESULTS AND DISCUSSION

The models for particle–gas drag, particle–liquid drag and liquid–gas interfacial drag can now be employed in conjunction with the force balances on the liquid and gas phases to predict the void fraction and the two-phase pressure drop. Elimination of the pressure gradient between [15] and [16] yields

$$\alpha(1-a) + \alpha F_{pL}^* - (1-\alpha)F_{pG}^* - F_i^* = 0. \qquad [54]$$

For given superficial velocities j_L and j_G, determination of the void fraction from [54] requires an iterative process. The iterative procedure is complicated by the fact that the drag forces depend on the flow regime and in turn on the void fraction. However, in this work the predictive procedure is simplified by assuming that j_L and α are given. Knowing α the relative permeabilities k_L, k_G, η_L and η_G and the viscous and inertial drag coefficients can be evaluated. Once this has been accomplished [54] becomes a quadratic equation in the superficial gas velocity j_G. One of the two roots of the equation is physically realistic and corresponds to positive values of j_G. The other root is a parasitic one which yields negative values of j_G. This root is discarded. Using the above procedure a curve of j_G vs α can be generated for a fixed liquid superficial velocity. The pressure gradient can be calculated using either [15] and [16] or by adding the two equations to yield

$$P^* = \frac{(1-\alpha+\rho^*\alpha)}{(1-\rho^*)} + F_{pL}^* + F_{pG}^*. \qquad [55]$$

In the above equation, the first term simply represents the hydrostatic head of the two-phase mixture and the second and third terms represent the particle drag on the two phases.

Co-current Flow ($j_L \geq 0$)

Figure 3 shows the void fraction and pressure gradient as functions of the gas superficial velocity for a particle diameter of 19 mm. Two sets of results corresponding to liquid superficial velocities of 0 and 9.15 mm/s are plotted as solid and dashed lines, respectively. Also plotted in figure 3 are data from Chu *et al.* (1983) under the same conditions. Initially the void fraction can be seen to increase very rapidly with increasing j_G for a fixed liquid flowrate. However, the increase in void fraction α tends to slow down at higher j_G. Furthermore, for a given j_G it can be seen that α decreases slightly with an increase in liquid flowrate. This is consistent with Dhir's (1984) model based on the drift flux approach. For the case of zero liquid flowrate, the pressure gradient initially decreases rapidly with an increase in the gas flowrate. The decrease results from a reduction in the hydrostatic head as the void fraction increases. At higher gas flowrates, an increase in particle drag compensates for the reduction in hydrostatic head and the overall pressure gradient remains fairly constant over a large range of gas flowrates. Here it should be mentioned that steady-state operation at zero liquid flowrate is possible only up to the onset of annular flow. At a liquid flowrate of 9.15 mm/s, the observed pressure gradient initially shows a behavior similar to the zero liquid flowrate case. However, as the gas velocities are increased further the particle drag increases at a rate faster than the reduction in hydrostatic head. As a result the overall pressure gradient goes through a local minimum at a gas superficial velocity of 0.26 m/s. The predictions are within 10% of the void fraction and pressure gradient data obtained for liquid flowrates in the range 0 – 20 mm/s and gas flowrates in the range 0–1.5 m/s.

Figure 4 shows the void fraction and pressure gradient as functions of the gas superficial velocity for a particle diameter of 9.9 mm. Again predictions along with the data from Chu *et al.* (1983) are plotted for liquid velocities of 0 and 9.15 mm/s. Essentially, the same trends are observed for j_G dependence on void fraction and pressure gradient as were observed for the cases plotted in figure 3. However, at a liquid flowrate of 9.15 mm/s the particle drag becomes more pronounced at relatively low gas velocities for the smaller particles. Consequently, the local minimum in the pressure gradient is shifted to a gas velocity of 0.16 m/s compared to a value of 0.26 m/s for 19 mm particles. The prediction are seen to agree quite well with the data.

A comparison of the observed void fractions with those predicted from the present model and the model proposed by Dhir (1984) is made in figure 5. In Dhir's model a drift flux approach was used and unknown constants were adjusted empirically. In the present model a mechanistic approach is used which includes submodels for the particle–gas, particle–liquid and interfacial drags. The present model compares quite favorably with the data. The model proposed by Dhir generally predicts the void fractions within about 10% as long as the void fractions do not exceed the limit of the model ($\alpha < 0.6$).

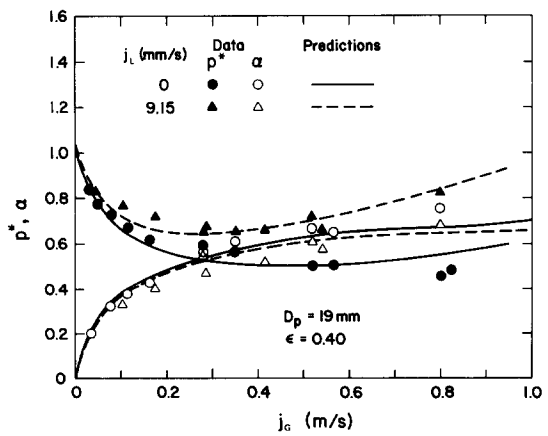

Figure 3. Comparison of predicted pressure gradient and void fraction with experimental data. Co-current flow, $D_p = 19$ mm.

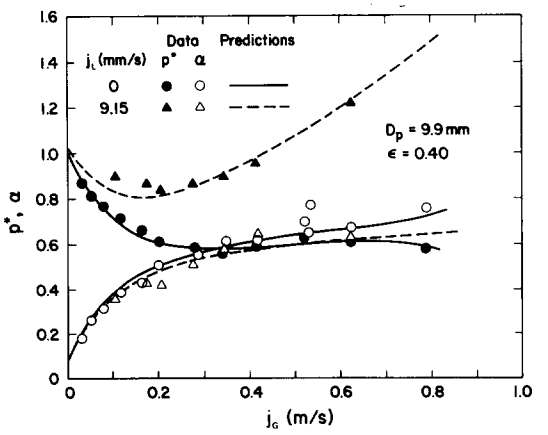

Figure 4. Comparison of predicted pressure gradient and void fraction with experimental data. Co-current flow, $D_p = 9.9$ mm.

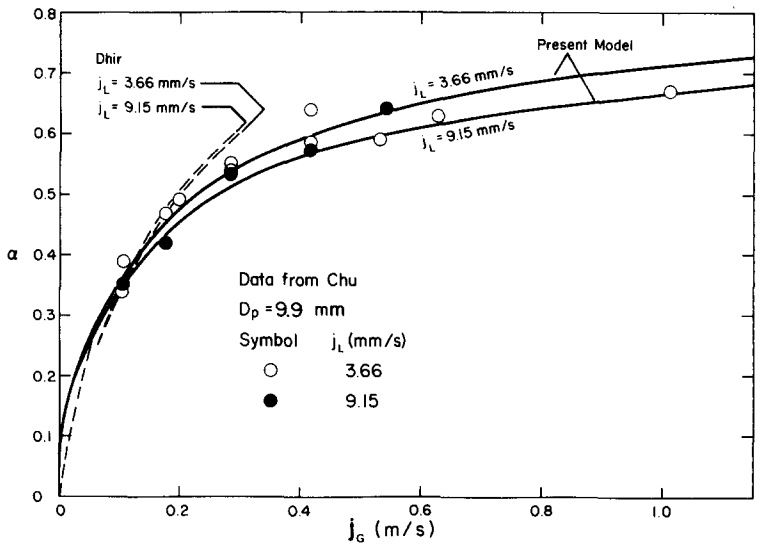

Figure 5. Comparison of observed void fraction with those predicted by Dhir (1984) and by the present model.

Counter-current Flow ($j_L \leqslant 0$)

Calculation of the void fraction and pressure gradient can be carried out in the same manner as in co-current flow except that liquid velocity is now negative. Figure 6 shows the predicted void fraction and pressure gradient as functions of gas flowrate for a particle diameter of 19 mm and liquid superficial velocities of -3.89 mm/s and -11.67 mm/s. The results corresponding to liquid flowrates of -3.89 mm/s and -11.67 mm/s are plotted as dashed and solid lines, respectively. Also plotted in figure 6 are void fraction and pressure gradient data obtained by Marshall & Dhir (1984) under the same liquid flowrates. As the superficial velocity of gas is increased, the void fraction initially increases very rapidly. The rate of increase however decreases with the superficial gas velocity until a critical gas velocity is reached. At this velocity a rapid increase in the void fraction is predicted. The critical gas velocity is generally referred to as the flooding velocity. The dimensionless pressure gradient shows a gradual drop until the flooding limit is reached. At the flooding limit a rapid drop in the pressure gradient is also predicted. The predictions from the present model compare well with the data of Marshall & Dhir (1984). The void fraction and pressure gradient data reported by Marshall & Dhir do not cover, however, the full span of gas flow rates for the cases shown in figure 6. As such, a comparison of the behavior near the flooding limit cannot be made.

Figures 7 and 8 show a comparison of the predicted and observed void fraction and pressure gradient in porous layers composed of 9.9 and 5.8 mm dia particles, respectively. The predictions compare reasonably well with the data. However, the model appears to over-predict the void

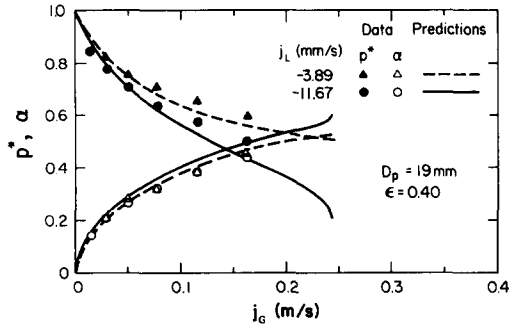

Figure 6. Comparison of predicted pressure gradient and void fraction with experimental data. Counter-current flow, $D_p = 19$ mm.

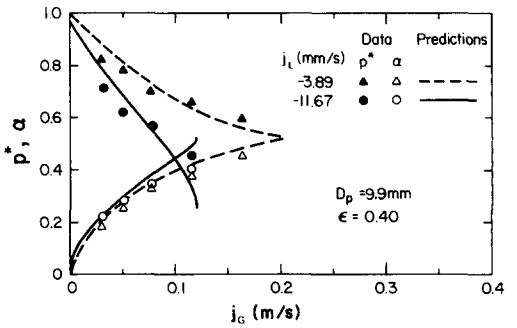

Figure 7. Comparison of predicted pressure gradient and void fraction with experimental data. Counter-current flow, $D_p = 9.9$ mm.

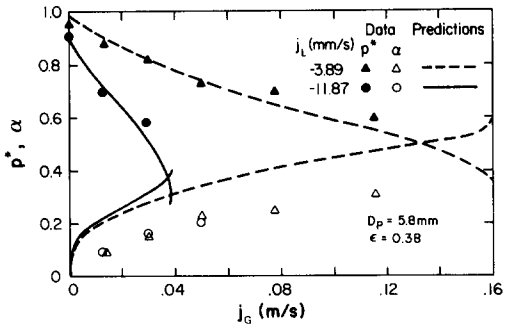

Figure 8. Comparison of predicted pressure gradient and void fraction with experimental data. Counter-current flow, $D_p = 5.8$ mm.

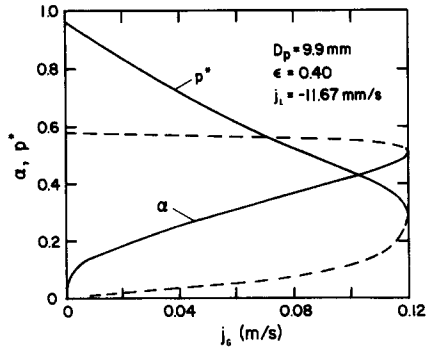

Figure 9. Typical variation of pressure gradient and void fraction with gas velocity in counter-current flow.

fraction for 5.8 mm dia particles. One probable reason for this difference between predictions from the model and the data could be that in the experiment the void data have been over-corrected for the presence of nonactive voids in the porous layer.

Counter-current Flooding Limit

Under the influence of gravity, the flooding limit represents the maximum possible gas flowrate for a fixed liquid flowrate or vice versa. This limit is of interest in many chemical and nuclear applications—some of which were discussed earlier. Using the counter-current flooding data of Sherwood *et al.* (1938) and Lobo *et al.* (1946) obtained with large rashig rings, Wallis (1969) developed a correlation for the flooding limit in porous layers:

$$j_G^{*1/2} + j_L^{*1/2} = 0.775. \quad [56]$$

In the above equation j_k^* is the dimensionless superficial velocity of each phase and is defined as

$$j_k^* = |j_k| \left[\frac{6(1-\epsilon)\rho_k}{\epsilon^3 D_p g(\rho_L - \rho_G)} \right]^{1/2}. \quad [57]$$

As has been discussed by Wallis (1969), the correlation obtained by Dell & Pratt (1951) based on their counter-current flooding data in a liquid–liquid system can be reduced to the same form as [56] but with slightly different empirical constants.

Marshall & Dhir (1984) experimentally investigated flooding limits in porous layers composed of spherical particles. In their experiments water and air were used as the denser and lighter fluids, respectively. The counter current flooding data covering a range of particles from 5.8 to 19 mm were correlated with an equation similar to [56] but with a constant of 0.875 on the r.h.s. The data were in the range of $0.15 \leqslant j_L^{*1/2} \leqslant 0.73$. Counter-current flooding in porous media composed of spherical particles with steam and water as test fluids was experimentally studied by Schrock *et al.* (1984). For liquid superficial velocities in the range of $0 \leqslant j_L^{*1/2} \leqslant 0.45$, Schrock *et al.* correlated their data as

$$j_G^{*0.38} + 0.95 j_L^{*0.38} = 1.075. \quad [58]$$

In [56]–[58], the superficial velocities are nondimensionalized with the assumption that the inertial drag is balanced by the hydrostatic head. Such nondimensionalization has physical significance only when inertial terms in the Kozeny–Carman equation dominate. For low superficial velocities, where viscous drag dominates, the dimensionless form of the superficial velocities as given by [57] is merely a convenience. For this reason it is no surprise that for low superficial liquid velocities, Schrock *et al.* (1984) correlated their data with different exponents on the superficial velocities than did Marshall & Dhir (1984) and Wallis (1969).

The present model includes both viscous and inertial terms in the particle–gas, particle–liquid and liquid–gas drags and as such can be used to predict the flooding limits over the whole range of flow velocities.

Figure 9 shows the predicted pressure drop and void fraction as functions of gas flowrates for

a particle diameter of 9.9 mm and a liquid superficial velocity of -11.67 mm/s. It is seen from figure 9 that for a given value of j_G, two sets of operating conditions (as denoted by the solid and dashed lines) are possible. The solid lines indicate an increase in void fraction accompanied by a decrease in pressure drop as j_G is increased. This behavior is similar to that shown by Marshall & Dhir's (1984) data. The dashed lines, however, indicate the opposite trends of decreasing void fraction and increasing pressure drop as j_G is increased. The behavior is similar to that observed by White (1935) and Elgin & Weiss (1939). Actual behavior of the data consistent with either of the two branches of the solution depends on the manner in which the flooding experiments are conducted. In Marshall & Dhir's experiments water was drained through a liquid-filled lower plenum such that water occupied all the bed area not filled by gas. Thus in their experiments, the operating point at $j_G = 0$ always began with a zero void fraction, as shown by the solid lines. White (1935) and Elgin & Weiss (1939), on the other hand, conducted experiments in which liquid was drained into a gas-filled lower plenum. As such, in their experiments a nonzero void fraction existed even with $j_G = 0$; this is shown by the dashed lines. From an application point of view, the experimental approach used by Marshall & Dhir corresponds to physical situations in which dryout is approached from a liquid saturated condition in the porous layer. Likewise, White and Elgin & Weiss' experiments correspond to physical situations similar to quenching of porous layers which are initially devoid of any liquid presence.

The two branches of the solution, however, coincide at $j_G = 0.12$ m/s, where both void fraction and pressure drop exhibit infinite slopes with respect to j_G. This point represents the flooding limit, since no solution is possible if j_G is increased beyond this value.

Just prior to the onset of flooding the pressure gradient and void fraction show a rapid change. In the experiments of Marshall & Dhir, the air flowrate was increased in steps while the liquid flow rate was kept constant. On approaching flooding they observed a faster increase in the level of the liquid–gas mixture above the porous layer. This indicates that the void fraction in the bed also increases at a faster rate, resulting in displacement of liquid by the gas. Interestingly, the predictions shown by the dashed lines in figure 9 indicate very little change in the void fraction for almost the entire range of gas flowrates except near the flooding limit. This trend is in complete agreement with experimental observations reported by Elgin & Weiss (1939). The pressure drop corresponding to the dashed line in figure 9 is also plotted on a log–log scale in figure 10. The predictions indicate that the pressure drop varies almost like j_G^2 for a large range of gas flowrates. However, as the flooding limit is approached, a break point occurs at about 80% of the value of j_G at the flooding limit. Beyond this breakpoint, the pressure drop shows a much stronger dependence on j_G. This is again in agreement with the observations reported by White (1935). In fact, White (1935) specified this breaking point experimentally as the loading point.

Figure 11 shows the various dimensionless forces acting on the two phases for the parameters corresponding to figure 9. For the solution shown by the solid line the particle–liquid drag can be seen to increase monotonically with j_G, and has an infinite slope at the flooding limit. The particle–gas drag increases very rapidly at small j_G and α due to the α^3 term is the relative permeabilities. It reaches a maximum value at $j_G \simeq 0.015$ m/s and then decreases monotonically since the flow area (α) increases at a rate faster than j_G^2. In a large range of j_G near the flooding limit the particle–gas drag, however, remains fairly constant. The interfacial drag initially increases with j_G due to an increase in the interfacial area associated with an increase in the void fraction. However, at higher void fractions, the term $(1-\alpha)^3$ in the drag coefficient results in a decrease in the interfacial drag. Figure 11 shows that for $j_G > 0.06$ m/s, the interfacial drag can be more than twice the particle–gas drag. As such, neglect of this term can result in serious errors in the predictions.

Figure 12 shows a comparison of the flooding limits predicted from the present model with the data reported by Marshall & Dhir (1984). The agreement can be seen to be very good except in the range of smaller liquid flowrates. Here, it should be noted that measurements of the flooding limits at low flow velocities are exceedingly difficult due to the fact that a small variation in liquid flowrate can result in a large variation in gas velocity. A larger scatter in data at low superficial velocities is thus expected.

Figure 13 shows the predictions for the relationship between j_L^* and j_G^* at flooding for porous layers formed of 5.8 and 19 mm dia particles. In this figure the correlations of Wallis (1969),

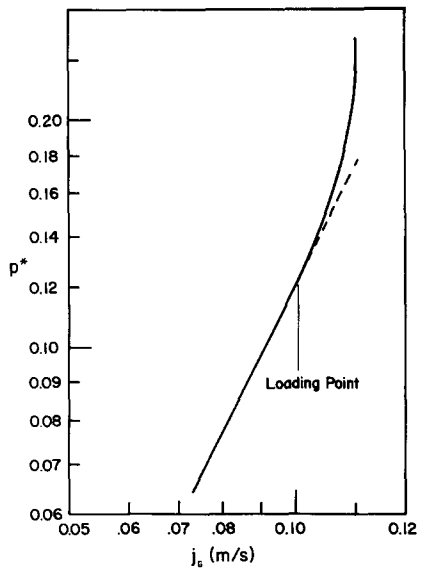

Figure 10. Logarithmic plot of pressure gradient vs gas velocity corresponding to the set of solutions shown by the dashed lines in figure 9.

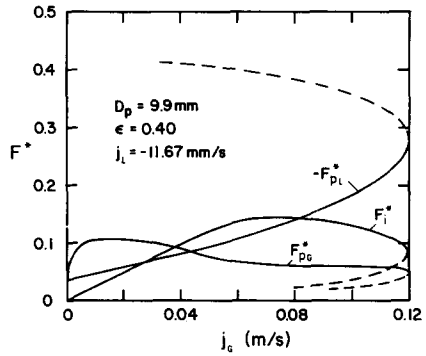

Figure 11. Typical variation of drag forces with gas velocity in counter-current flow.

Schrock *et al.* (1984) and Marshall & Dhir (1984) are also plotted. The predictions from the present model follow the correlation of Schrock *et al.* (1984) and Marshall & Dhir (1984) very closely in their respective ranges of data. The correlation of Wallis generally tends to give slightly lower values. The present model shows a rather weak dependence of the flooding limits on the particle size apart from what is already included in the nondimensionalization of the velocities. At low superficial liquid or gas velocities, viscous effects dominate and as such the predictions show a nonlinear variation of $j_G^{*1/2}$ with $j_L^{*1/2}$. At moderate flow velocities, however, the predictions show a nearly linear dependence of $j_G^{*1/2}$ with $j_L^{*1/2}$, especially when a mean of the predictions for the two extreme size particles is considered. The predictions thus point out that for moderate superficial gas and liquid velocities, the form of correlations employed by Wallis (1969) and Marshall & Dhir (1984) is correct. However, at low superficial gas or liquid velocities, correlations of the type given by Schrock *et al.* (1984) will be more appropriate.

Flow Regime Map

The predictions from the present models for the flow configurations can be compared with the data. This is done in figure 14 for co-flow of air and water through a particulate layer composed

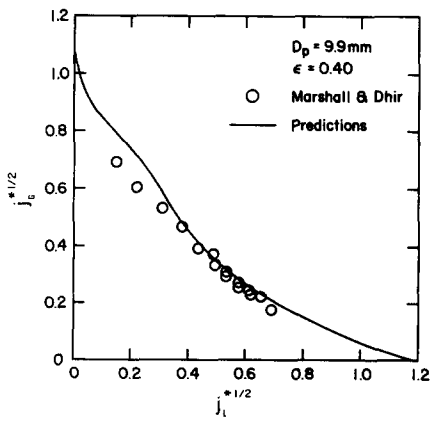

Figure 12. Comparison of predicted flooding limits with existing experimental data.

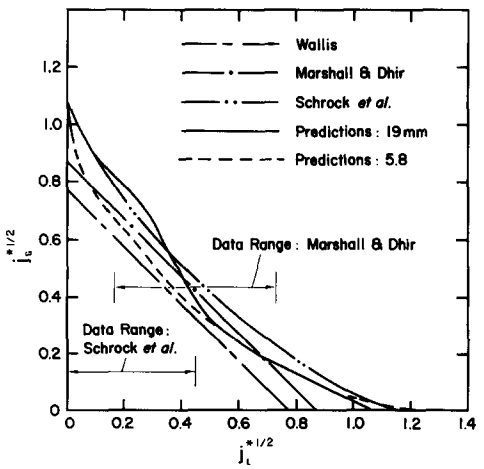

Figure 13. Comparison of predicted flooding limits with existing correlations.

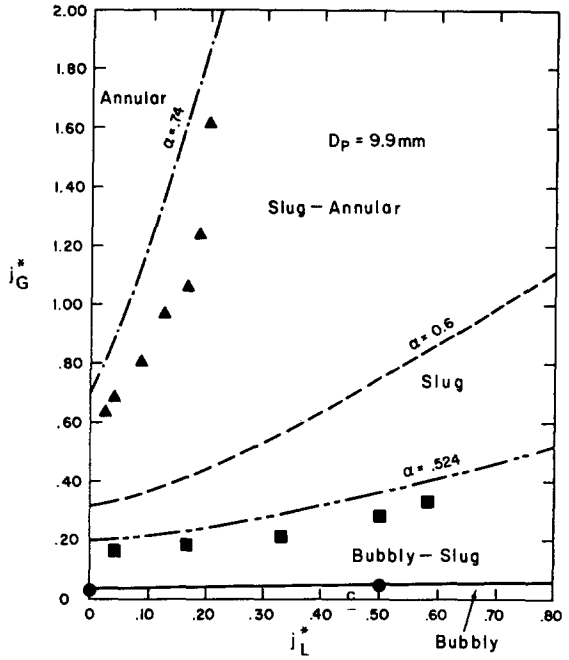

Figure 14. Comparison of observed and predicted flow regimes in co-current flow.

of 9.9 mm dia particles. In this figure the data for the transitions from bubbly to bubbly-slug flow, bubbly-slug to slug flow and slug-annular to annular flow are also plotted. The predictions compare quite well with the data considering the fact that the transitions were recognized visually and the transitions based on the model are quite sensitive to the chosen value of the void fraction.

The flow regimes that exist in the porous layers at the onset of counter-current flooding are given in table 1. The predictions are made for particles of 19, 9.9 and 5.8 mm dia and the tabulated values are for the range of $j_L^{*1/2}$ in a given regime. It is noted that for a given particle size, the flow regimes at flooding are sensitive to the superficial liquid or gas velocities. As a result, flooding can occur in bubbly, slug or annular flow. Similarly, for a fixed superficial liquid velocity, the flow regime at flooding can be particle size dependent. For example, at $j_L^{*1/2} = 1$, bubbly flow will exist in 9.9 and 19 mm dia particles but it will be bubbly slug flow in 5.8 mm dia particles. Nevertheless, the dependence of flow regime on particle size is weak.

4. CONCLUSIONS

(i) Flow regimes have been identified through simple geometric models and predictions for co-current and counter-current flow compare reasonably well with the data.

(ii) Models for particle–gas, particle–liquid and liquid–gas interfacial drag have been developed. The models when incorporated in the force balance for the two phases, can be used to predict the pressure gradient and void fraction.

Table 1. Predicted flow regimes at flooding

	$j_L^{*1/2}$		
Flow regime	$D_p = 19$ mm	$D_p = 9.9$ mm	$D_p = 5.8$ mm
Bubbly	0.83–1.07	0.91–1.22	1.13–1.24
Bubbly-slug	0.55–0.83	0.49–0.91	0.44–1.13
Pure slug	0.45–0.55	0.40–0.49	0.33–0.44
Slug-annular	0.21–0.45	0.17–0.40	0.11–0.33
Pure annular	0–0.21	0–0.17	0–0.11

(iii) Predictions of the pressure gradient and void fraction for co-current flow are within 10% of the data. For counter-current flow, the predictions can deviate by as much as 15% when the particles are not very large.

(iv) The present model has been employed to predict counter-current flooding limits in porous layers composed of particles varying in size from 5.8 to 19 mm dia. Predictions are found to agree well with the existing flooding correlations and data.

(v) The model shows that two counter-current sets of operating conditions are possible in flooding experiments. Conflicting behavior of void fraction and pressure drop reported by various investigators has thus been resolved by the present model.

Acknowledgement—This work received partial support from EPRI under Contract No. RP-1931-1.

REFERENCES

CHU, W., DHIR, V. K. & MARSHALL, J. S. 1983 Study of pressure drop, void fraction and relative permeabilities of two phase flow through porous media. Presented at *21st natn. Heat Transfer Conf.*, Seattle, Wash. *AIChE Symp. Ser. No.* 225 **79,** 224–235.

DELL, F. R. & PRATT, H. R. C. 1951 Flooding rates for packed columns. *Trans Instn Chem. Engrs* **29,** 89–109.

DHIR, V. K. 1984 Some aspects of two phase flow through porous media. In *Proc. Japan–US Semin. on Two Phase Flow Dynamics*, Lake Placid, N.Y.

DHIR, V. K. & BARLEON, L. 1981 Dryout heat flux in a bottom heated porous layer. *Am. nucl. Soc. Trans.* **38,** 385–386.

ELGIN, J. C. & WEISS, F. B. 1939 Liquid holdup and flooding in packed towers. *Ind. Engng Chem.* **31,** 435–445.

HARDEE, H. C. & NILSON, R. H. 1977 Natural convection in porous media with heat generation. *Nucl. Sci. Engng* **63,** 119–132.

ISHII, M. & CHAWLA, T. C. 1979 Local drag laws in dispersed two-phase flow. Report NUREG/CR-1230.

JONES, S. W., EPSTEIN, M., GABOR, J. D., CASSULO, J. C. & BANKOFF, S. G. 1980 Investigation of limiting boiling heat fluxes from debris beds. *Am. nucl. Soc. Trans.* **35,** 361–362.

LAMB, H. 1932 *Hydrodynamics*, 6th edn, p. 604. Cambridge Univ. Press, Cambs.

LIPINSKI, R. J. 1981 A one dimensional particle bed dryout model. *Am. nucl. Soc. Trans.* **38,** 386–387.

LIPINSKI, R. J. 1984 A coolability model for post accident nuclear reactor debris. *Nucl. Technol.* **65,** 53–66.

LOBO, W. E., FRIEND, L., HASHMALL, F. & ZENZ, F. 1946 Limiting capacity of dumped tower packing. *AIChE Trans.* **41,** 693–710.

MARSHALL, J. S. & DHIR, V. K. 1984 Hydrodynamics of counter-current two phase flow through porous media. Report NUREG/CR-3995.

NAIK, A. S. & DHIR, V. K. 1982 Forced flow evaporative cooling of a volumetrically heated porous layer. *Int. J. Heat Mass Transfer* **25,** 541–552.

SCHEIDEGGER, A. E. 1960 *The Physics of Flow through Porous Media.* Macmillan, New York.

SCHROCK, V. E., WANG, C.-H., REVANKAR, S., WEI, L.-H., LEE, S. Y. & SQUARER, D. 1984 Flooding in particle beds and its role in dryout heat fluxes. In *Proc. 6th Information Exchange Mtg on Debris Coolability*, UCLA, Los Angeles, Calif.

SCHULENBERG, T. & MULLER, U. 1984 A refined model for the coolability of core debris with flow entry from the bottom. In *Proc. 6th Information Exchange Mtg on Debris Coolability*, UCLA, Los Angeles, Calif.

SHERWOOD, T. K., SHIPLEY, G. H. & HOLLOWAY, F. A. L. 1938 Flooding velocities in packed columns. *Ind. Engng Chem.* **30,** 765–769.

TUNG, V. X., DHIR, V. K. & SQUARER, D. 1983 *Forced Flow Cooling Studies of Volumetrically Heated Porous Layers.* Therm. Hydr. Nucl. Reactors, Santa Barbara, Calif.

TUTU, N. K., GINSBERG, T. & CHEN, J. C. 1983 Interfacial drag for two phase flow through high permeability porous beds. Presented at *21st National Heat Transfer Conf.*, Seattle, Wash.

VASILIEV, L. L. & MAIAROV, V. A. 1979 An analytical study of resistance, heat transfer and stability in evaporative cooling of a porous heat producing element. *Int. J. Heat Mass Transfer* **22,** 301–307.

WALLIS, G. B. 1969 *One Dimensional Two Phase Flow.* McGraw-Hill, New York.

WHITE, A. M. 1935 Pressure drop and loading velocities in packed towers. *Trans. AIChE* **31,** 390–408.

APPENDIX

Maximum Void Fraction Accommodated by the Particles' Surface (α_0)

The maximum number of bubbles which can be supported by the surface of particles can be obtained by dividing the surface area by the area required to support one single bubble. The void fraction α_0 then can be obtained simply as the ratio of gas volume to total pore volume. In the following analysis, certain assumptions about the geometry of the porous layer and flow configurations will be made.

- The particles are assumed to be formed as rhombic arrays with center-to-center distance greater than D_p. This assumption is, of course, only valid on an average basis. The average distance, d, between two adjacent particles than can be given as

$$\eta = \frac{d}{D_p} = \left[\frac{\pi\sqrt{2}}{6(1-\epsilon)}\right]^{1/3}. \qquad [A.1]$$

- The bubbles are crowded onto the surface of the particles as square arrays. The distance between two adjacent bubbles varies between D_b and $2D_b$. In the present model, a value of $\sqrt{3}D_b$ is chosen as the typical value of the side of the square arrays. The area required to accommodate one single bubble is thus given as

$$A_b = 3D_b^2. \qquad [A.2]$$

Figure A.1 shows a typical arrangement of two adjacent particles. The cross-hatched area represents the area inaccessible by the bubbles. The lost area for one particle can be given as

$$A_1 = \frac{\pi}{2}(1+\gamma)(1+\gamma-\eta)D_p^2, \qquad [A.3]$$

where γ is the diameter ratio between bubbles and particles and η is given by [A.1]. Furthermore, in a rhombic array, each particle is in the proximity of 12 other particles. Therefore, the maximum number of bubbles which can remain on the surface of one single particle is given by

$$N = \frac{\pi}{3}\frac{1+\gamma}{\gamma^2}[6\eta - 5(1+\gamma)]. \qquad [A.4]$$

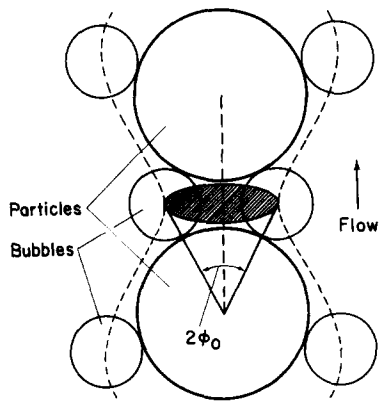

Figure A.1. Bubble flow path along the surface of the particles.

This number of bubbles, when multiplied by the volume of each bubble and divided by the average pore volume seen by each particle, yields the following relation for α_0:

$$\alpha_0 = \frac{\pi}{3}\frac{(1-\epsilon)}{\epsilon}\gamma(1+\gamma)[6\eta - 5(1+\gamma)] \quad \text{as long as} \quad \alpha_0 \geqslant 0. \qquad [A.5]$$

Maximum Void Fraction Without Merging of Bubbles (α_I)

Consider the gas bubble as another solid particle with diameter D_b. Marshall & Dhir (1984) have shown that the minimum porosity for such a binary mixture is given by

$$\epsilon_{sat} = 0.40 - 0.24(1-\gamma)^2. \qquad [A.6]$$

The minimum porosity ϵ_{sat}, however, simply represents the liquid volume contained in one unit volume of the porous layer. Therefore,

$$\epsilon_{sat} = \epsilon(1-\alpha_I). \qquad [A.7]$$

For porous layers composed of spherical particles, the porosity is nearly 0.40. Therefore, by combining [A.6] and [A.7] one obtains

$$\alpha_I = 0.60(1-\gamma)^2. \qquad [A.8]$$

In the limit as $\gamma \to 0$ flow in the pores will be similar to that in tubes. Therefore, the applicability of [A.8] will be limited to $\alpha_I \leqslant 0.30$. When $\gamma \leqslant 0.29$, the transition void fraction α_I will be taken to be 0.30, similar to that in tube flows.